COMMUNICATIONS IN SCIENCE AND TECHNOLOGY
Homepage: cst.kipmi.or.id

Three-dimensional pore structure of activated carbon monolithic derived from hierarchically bamboo stem for supercapacitor application

Erman Taer[a*], Lini Pratiwi[a], Apriwandi[a], Widya Sinta Mustika[a], Rika Taslim[b], Agustino[a]

[a]*Department of Physics, University of Riau, 28293 Simpang Baru, Riau, Indonesia*
[b]*Department of Industrial Engineering, State Islamic University of Sultan Syarif Kasim, 28293 Simpang Baru, Riau, Indonesia*

Article history:
Received: 20 May 2020 / Received in revised form: 29 May 2020 / Accepted: 31 May 2020

Abstract

A three-dimensional pore structure on activated carbon derived from hierarchically bamboo stem was synthesized in the monolithic form for increased applicability as a supercapacitor electrode. The preparation involved two step carbonizations, using a chemical activation at different concentrations. Subsequently, the morphology, chemical content, specific surface area and pore size distribution, as well as crystalline degree were evaluated with scanning electron microscopy, energy X-ray (EDX), N_2 sorption and X-ray diffraction, respectively. Therefore, cyclic voltammetry (CV) was used to assess the electrochemical performance, in a two electrode system. The result shows the significant impact of the three-dimensional structure on electrochemical performance, and the optimized sample exhibited specific capacitance of 168.8 F g^{-1}, energy density of 23.44 Wh kg^{-1}, and power density of 84.46 W kg^{-1}.

Keywords: Activated carbon, bamboo stem, monolitich, three-dimensional structure, supercapacitor

1. Introduction

Supercapacitors are attractive energy strategies for reducing environmental pollution from fossil fuel exploitation. This technology is characterized by high energy/power, high charge/discharge rate, and long cycle life [1], and are generally classified into two energy storage mechanism, including (1) pseudo-capacitance with faradic redox. (2) Electrochemical double layer capacitance (EDLC) devoid of faradic redox [2], also defined as an accumulation of ion pairs, compromising the electrostatic interaction with polarized electrodes [3]. This mechanism is affected by the electrode architecture and porous texture, hence the materials selected for use are of high importance [4]. There is rising interest in the use of carbon-based materials, including carbon aerogel [5], foam [6], fiber [7], nanotube [8], and graphite [9]. Particularly, activated carbon is suggested as an attractive resource, due to the sustainability, easy production and cost effectiveness [10].

Furthermore, precursor selection is a crucial process because the carbon sources influences the textural and structural characteristic as well as yield of the final product [11,12]. In addition, lignocellulosic biomass are the most commonly used activated carbon resources, due to the abundant availability, eco-friendliness, and processing versatility [13]. The major chemical composition include cellulose, hemicellulose and lignin, linked by C–O–C or C–C bonds [14]. Moreover, the average elemental constituent in hemicellulose include carbon (44.4 wt%), oxygen (49.4 wt%) and hydrogen (6.2 wt%). This composition is relatively similar to cellulose, while lignin consists of carbon (62 wt%) and oxygen (32 wt%) [15]. Furthermore, the biomass typically includes wood as a major component and grass [16].

For example, bamboo is a lignocellulosic-based material, comprising about 43.44% cellulose, 29.56% hemicellulose, and 27.52% lignin [17]. This contains a natural porous network, known to support the generation of three-dimensional (3D) pore structures [18], and also provide high ion transport [16]. Therefore, bamboo has been suggested as a supercapacitor electrode, and some reports show the fabrication into powder forms, under varied conditions, including temperature of carbonization [19] and activation [18,20], chemical treatment with KOH [18,21,22] or molten carbonate [23], as well as doping with heteroatom (S, N, B) [22,24,25]. Unfortunately, the phenomenon of dusting reduces mechanical strength, while binder materials lead to poor electrical conductivity and high production cost [2]. Therefore, free standing electrodes devoid of binder materials are necessary for further supercapacitor application.

The focus of previous studies has been limited to enhancing electrochemical performance, and there are only a few literatures discussing the application of activated carbon without binder as supercapacitor electrode. Some reports on binder-free electrodes consist of mixtures with a nanocomposite MnO_2 [26,27], leading to poor production cost effectiveness and electrical conductivity. Meanwhile, the monolith forms are recommended for the low cost and ease of processing binder free electrode, subsequently ensuring good mechanical strength and high electrical conductivity [2].

Therefore, in this study, we report on the synthesis of

* Corresponding author.
Email: erman.taer@lecturer.unri.ac.id

activated carbon from hierarchically bamboo stem in the monolithic form, to be used as binder free electrode for supercapacitor application. The raw material was first treated in two step carbonizations, followed by chemical activation using different concentrations (1 M and 3 M) of potassium hydroxide (KOH). Then, structure characterization to activated carbon monolithic were done using a scanning electron microscopy (SEM), N_2 gas sorption, X-ray diffraction (XRD), and energy X-ray (EDX). Furthermore, the electrochemical performance was then tested, using cyclic voltammetry (CV) in 1 M H_2SO_4 electrolyte, assembled in two electrode system. The effect of chemical activation of activated carbon monolithic on their density will also be discussed in detail. The effect of electrode thickness on their electrochemical performance also will be discussed in this study.

2. Materials and Methods

2.1 Monolithic Electrode Preparation

Green bamboo stem was collected in Riau province, Indonesia, and prepared into pellet formed with a diameter of around 3 cm, by cross sectional cutting. These were then dried in the oven at temperature at 110 ^oC for 48 hours, and activated through two-step carbonization, under a N_2 environment, as illustrated in Fig. 1. The first step involves the carbonization process, conducted through a multi-step heating temperature (Fig. 1(a)). This process was initiated at 30 ^oC (room temperature) and raised up to 339 °C, at a low heating rate of 1 ^oC/min, held for 1 hour. The material was then decomposed to produce higher carbon content.

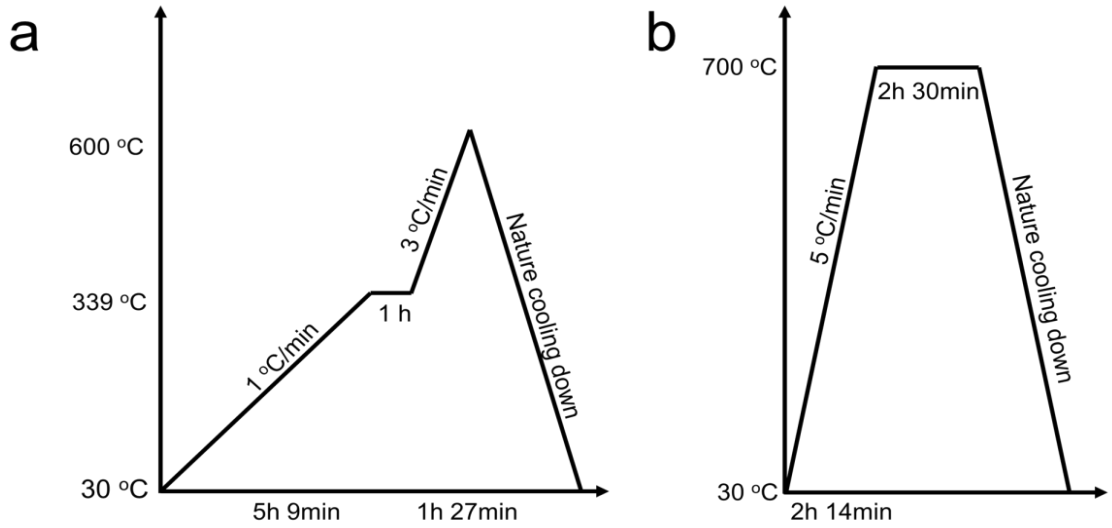

Fig. 1. Carbonization profile:; (a) first step carbonization; (b) second step carbonization.

Therefore, carbonization was continued to maximum temperature of 600 ^oC, featuring the reduction of some low molecular weight volatile components. The entire process was terminated by cooling naturally to room temperatures, hence the hierarchically bamboo carbon (HBC) is produced without binder.

Subsequently, the HBC samples were polished into a diameter of 0.8 cm, followed by chemical activation by immersing into potassium hydroxide (KOH) solution served at different concentration of 1 M and 3 M. Therefore, the hierarchically bamboo porous (HBP) based activated carbon monolith was produced and the samples were labeled HBP-s, where s denotes the specific KOH concentration. Figure 1(b) shows the carbonized profile for the second phase, which involved single-step heating at a high rate of 5 ^oC/min. This carbonization was initiated at 30 ^oC up to 700 ^oC, followed by soaking for 2.5 hours. Therefore, new pores were generated, and finally the activated carbon HBP-s was polished and washed with deionized to achieve neutral pH. However, the samples were polished with two varied thickness, of 0.3 and 0.2 mm, denoted HBP-sa and HBP-sb, respectively for electrode performance evaluation.

2.2 Structure Characteristic

The monolithic characteristics were assessed based on the parameters of mass, diameter, and thickness, which were subsequently calculated into density. These values were obtained to evaluate the changes in the first and second step carbonization process, while the morphology and chemical compositions were investigated using scanning electron microscopy (SEM)(JEOL-JSM-6510LA) and energy X-ray (EDX), respectively. In addition, the SEM image was derived at an accelerating voltage of 15 kV, with secondary electron image. The Brunauer-Emmett-Teller (BET) and Barret-Joiner-Halenda (BJH) methods were applied for observing specific surface area (S_{BET}) and pore size distribution (PSD), respectively. These were measured using N_2 gas sorption at temperature of 77.35 K, by employing the Quantachrome Instrument TouchWin Version 1.2.

The crystalline degree of HBP-s samples was observed using the X-ray diffraction (XRD) (Phillip X-Pert Pro PW3060/10), measured with Cu-Kα radiation (Kα=1.5418 Å) source in the 2θ scale range of 10-100^o. Furthermore, the XRD parameters, including interlayer spacing (*d*) and microcrystallites dimension was calculated using the respective equations.

$$n\lambda = 2\,d\,\sin\theta \quad (1)$$

$$L_c = 0.89\lambda/\beta\,\cos\theta_{002} \quad (2)$$

$$L_a = 1.94\lambda/\beta\,\cos\theta_{100} \quad (3)$$

Where, n denotes the mean diffraction order in value, with 1 as the maximum. λ is the X-ray wavelength for Cu-Kα at radiation of 1.5418 Å, while *d* was defined as the interlayer *d* spacing, where d_{002} and d_{100} respectively signify θ_{002} and θ_{100}. In addition, θ is the angle of reflection plane, at 002 and 100, respectively, while L_c and L_a is the mean crystallite dimension in Å along a line normal to the corresponding reflecting plane. The parameter β represents the full width at half-maximum of the plane 2θ, while θ is the scattering angles (degree).

2.3 Electrochemical Performance

Electrochemical performance was tested in a two electrode system, using Cyclic Voltametry (CV) (CV UR Rad-Er 5841, Materials Laboratory, Department of Physics, University of Riau, Indonesia). The supercapacitor cell was assembled in the form of sandwich layers, encompassing the body cell, isolator, current collector, electrode, separator, and liquid electrolyte, while the HBP-s samples served as electrodes, and were immersed in 1 M H_2SO_4 electrolyte for 2 days. The two electrodes were placed onto separate circle stainless steel, to serve as the current collector, with thickness of ∼ 0.4 mm, and duck eggshell was applied as a separator [28]. These components were then packaged with teflon and acrylic as isolator and body cell, respectively, and the supercapacitor cell was finally connected to operate and counter the CV instrument electrode port. In addition, the CV measurement was performed at a voltage range of 0.0 to 1.0 V, and the data was recorded using Cyclic Voltammetry graphical user interface (CVv6). This apparatus was previously calibrated to VersaStat II Princeton Applied Research, with an error of ±6.05 %.

The sample electrochemical properties, including the specific capacitance, energy and power densities were evaluated by calculating the CV data, using the respective equations.

$$C_{sp} = \frac{I_c - I_d}{m\,x\,s} \quad (4)$$

$$E = \frac{1}{2} C_{sp}\,\Delta V^2\,x\,\frac{1000}{3600} \quad (5)$$

$$P = \frac{E}{\Delta t/3600} \quad (6)$$

Where C_{sp} denotes specific capacitance (F g^{-1}), I_c and I_d respectively signify the charge and discharge current (A), *m* served as the average mass loading of two electrodes (g), and *E* represents the average energy density of the electrode (Wh kg^{-1}). Also, ΔV and Δt respectively designate the potential window of CV (V) and clearance time in the discharge process (s), while *P* is the electrode average power density (W kg^{-1}).

3. Results and Discussion

3.1 Mass, Diameter, Thickness, and Density

The average mass of HBP-s pellet prior to the carbonization process was recorded as 1.174 and 0.912 g respectively for HBP-1 and HBP-3. Furthermore, a 60-64 % decline was observed without chemical activation at temperature of 600 ºC (Step-1). These mass losses were attributed to the release of low molecular volatiles, including oxygen, hydrogen and nitrogen during treatment. The pellet diameter also decreased from ~3 cm to ~1.65 cm after step-1, resulting from carbon atom rearrangement. Also, the average mass, thickness, diameter and density of all 20 duplicate samples were recorded after treatment at 600 ºC (Step-1) and 700 ºC (Step-2). Table 1 shows the continuous data at similar thickness with varied KOH concentrations, and the decline in density recorded after step-2 for HBP-1 and HBP-3 was attributed to mass loss and volume shrinkage. The carbonization temperature of 700 ºC also assisted the chemical activation to etch some carbon chains and leave some numerous vacancies [11]. These vacancies instigate carbon atom rearrangement, leading to a decline in pellet diameter. Moreover, density shrinkage also signify pore generation and porosity development, and this ensures better ion diffusion and improved electrochemical performance [29].

Table 1. Average mass, thickness, diameter and density.

Parameters	HBP-1		HBP-3	
	Step-1	Step-2	Step-1	Step-2
Mass (g)	0.106	0.095	0.095	0.090
Thickness (cm)	0.083	0.080	0.080	0.080
Diameter (cm)	1.663	1.651	1.585	1.513
Density (g/cm^3)	0.605	0.554	0.599	0.564

3.2 Scanning Electron Microscopy

Fig. 2 shows the morphology and structure of carbon samples observed through scanning electron microscopy (SEM). This parameter was influenced by the nature of raw materials selected, chemical activating agent used and the other treatment in the production of activated carbon. In addition, treatments in Step-1 cause carbon atom rearrangements, due to the release of low molecular weight volatiles, including oxygen, hydrogen and nitrogen, into the gaseous phase [11]. Subsequently, the chemical activation with KOH generates new pores during Step-2 carbonization [30].

Fig. 2(a) shows the cube-like three-dimensional hierarchical structure of HBP-1 [18,31], with maximum and minimum size of around 17.28 X 10 µm and 20.41 X 57.70 µm. These materials are covered by some walls, which subsequently contribute to pore blocking. In addition, KOH activation also results in some new pore formations on the cube surfaces, measuring around ~200 nm. Fig. 2(b) shows the characteristic rough surfaces of HBP-1, as shown by the marked region, indicating the limitations of 1 M KOH activation to carbon bound etching in bubble forms, and not proper pore development.

Fig. 2(c) showed the HBP structural modification caused by the highly alkaline 3M KOH. Based on the measurements, hierarchical cubes are larger than HBP-1, with a size range of 21.73 X 26.02 µm and 25.81 X 76.22 µm for the minimum

and maximum cubes, respectively. The incidence of pore blocking was also reduced by collapsing the covered walls. In addition, HBP-3 exhibits a greater number of new pores formed on the hierarchical cubes surface, with larger size in the macropore range of around ~400 nm, possibly serving as a channel for ion diffusion into the deeper pore [32]. Furthermore, the 3 M KOH activation also successfully generated new pores, as shown by the marked region of Fig.2 (d), and sample HBP-3 presents with a smooth surface, assumed to provide larger specific surface area compared to HBP-1. Also, HBP-3 achieved a unique flake structure, believed to ensure better electrical conductivity [33,34], and provide better electrochemical performance as predicted.

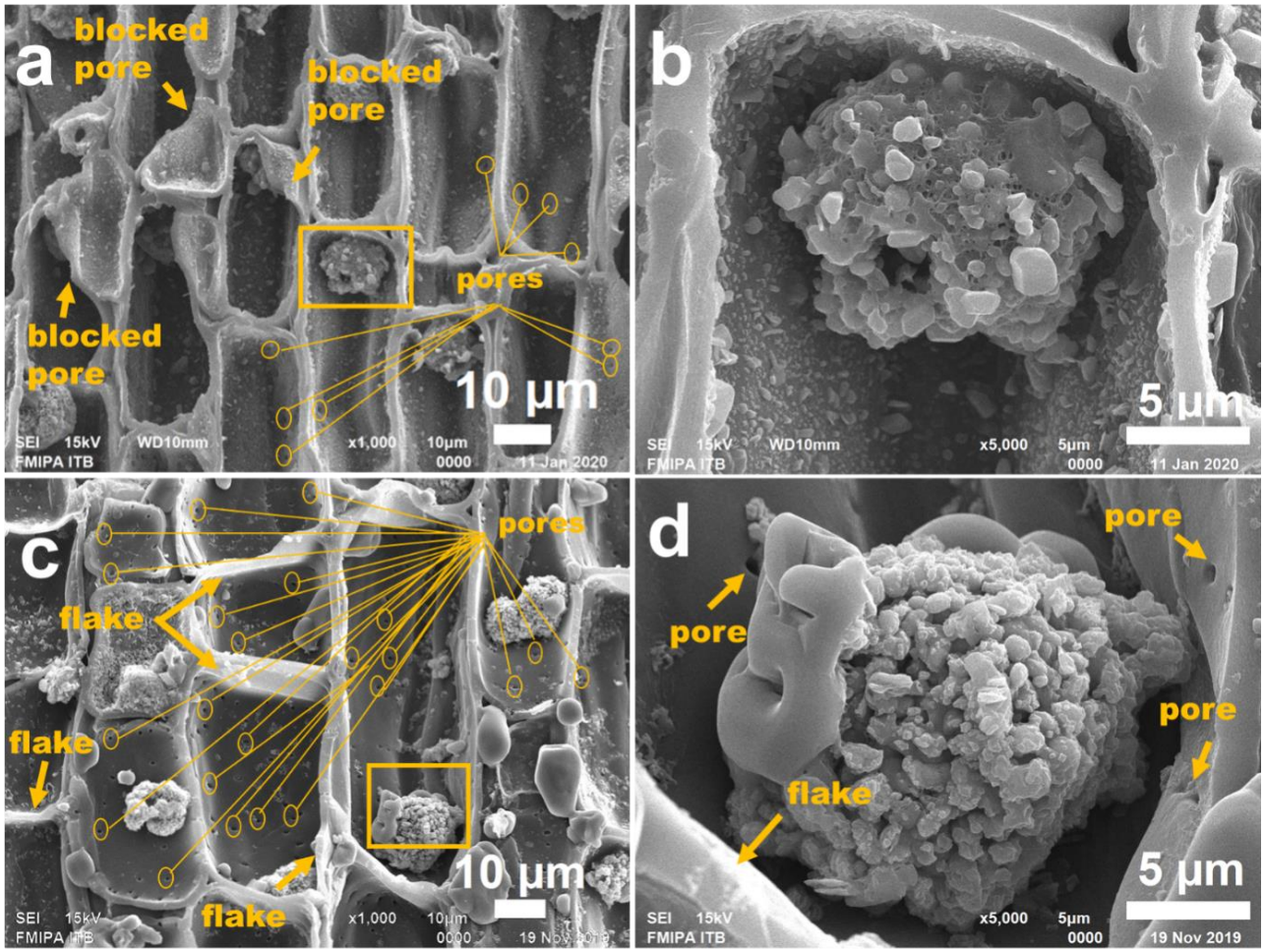

Fig. 2. SEM images of samples:. (a) HBP-1; (b) is the enlarged image of the selected region in (a); (c) HBP-3; (d) is the enlarged image of the selected region in (c).

3.3 N_2 Sorptions

Fig. 3 shows the N_2 adsorption/desorption isotherms from HBP-s samples. These were identified according to the international union of pure and applied chemists (IUPAC), as type IV as well as mesopores sorption [32]. Fig. 3(a) depicts the crossed neck of hysteresis at relative pressure ~0.4 P/P_0 in HBP-1, associated with the ink bottle pore shape induced pore blocking [35]. Fig. 3(b) shows the isotherm broad knee of hysteresis for HBP-3, affiliated with widening mesopore development [36]. In addition, Equation (6) depicts the chemical activation mechanism of carbon materials with KOH, where K-bound and K_2CO_3-occupied are removed by washing. This phenomenon consequently results in the generation of numerous new micropore vacancies [2]. The strong alkaline activation possibly produce larger pores [26], as evidenced by the BHJ methods (not seen here), where higher KOH concentration led to mesopore formation. These obviously measured 3.27 nm and 3.57 nm for HBP-1 and HBP-3, respectively.

$$6KOH + 2C \rightarrow 2K + 3H_2 + 2K_2CO_3 \quad (6)$$

Table 2 shows a summary of HBP-s sample textural properties, where higher KOH concentrations significantly increase the specific surface area (S_{BET}) from 2.04 to 154.65 $m^2\ g^{-1}$. However, a decline was observed for mesopores (S_{MESO}), and also in terms of volume (V_{MESO}). These results indicate the ability for 1 M KOH activation to generate very little amount of micropores in HBP-1, while more are created in treatments with 3 M KOH, leading to the improved specific surface area observed in HBP-3. Furthermore, HBP-1 demonstrated a large average diameter (D_{AVE}) of about ~17 nm, indicating the possibility that 1 M KOH activation only opened the hierarchical pore. However, HBP-3 exhibited an average pore diameter of ~2.2 nm, typical to mesopores, and presented in the narrow gap of micropores. This arrangement improves the suitability for ion storage, and the consequent increase in electrochemical performance.

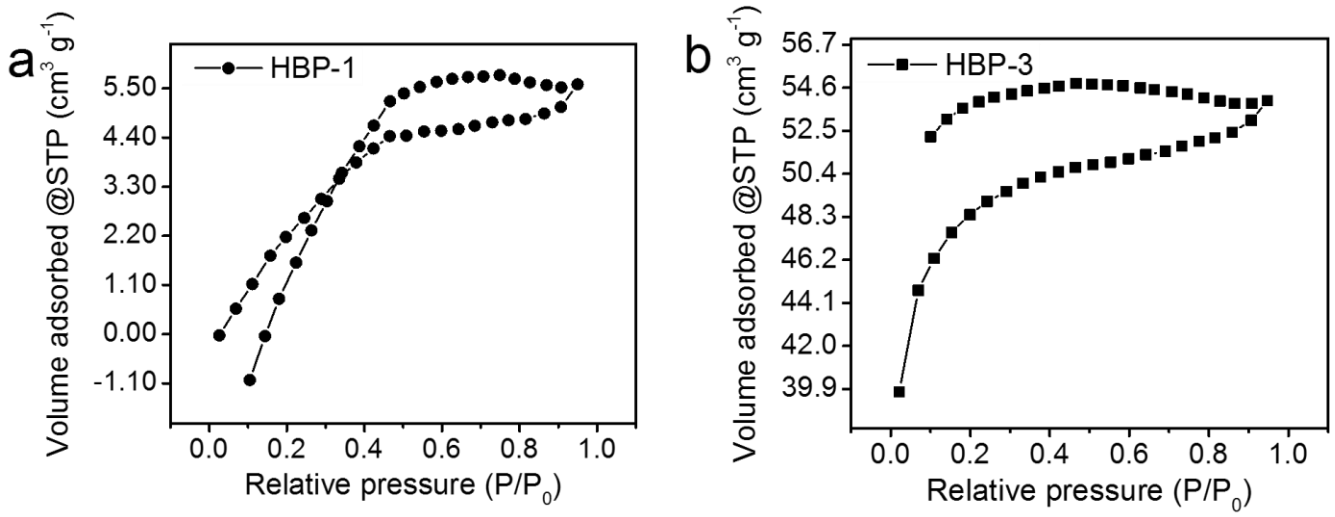

Fig. 3. The N_2 adsorption/desorption isotherms: (a) HBP-1; (b) HBP-3.

Table 2. Textural properties of monolithic activated carbon from HBP-s

Samples	S_{BET} ($m^2\ g^{-1}$)	S_{MESO} ($m^2\ g^{-1}$)	V_{MESO} ($cm^3\ g^{-1}$)	D_{AVE} (nm)
HBP-1	2.0400	5.3589	0.0050	17.0024
HBP-3	154.646	0.8950	0.0008	2.1644

3.4 X-ray Diffraction

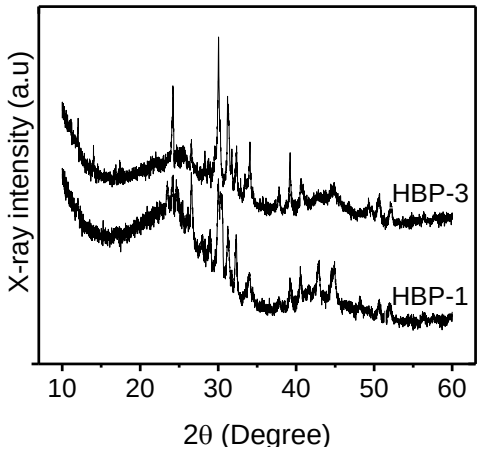

Fig. 4. XRD diffractogram of activated carbon monolith derived HBP-s samples

Fig. 4 shows the X-ray diffractogram of HBP-s crystalline structure, and two broad peaks were obtained at scattering angles (*2θ*, precisely 24-25° and 44-46°, reflecting the typical amorphous carbon planes of 002 and 100, respectively. Furthermore, activated carbon from pine bark was used as a reference, and the amorphous content was around 2θ to 23° (002) and 44° (100) [37]. The activated carbon electrode derived bamboo shoot also demonstrated two broad refection peaks at 18-26° and 42–45° under different carbonization temperature [38], where the amorphous carbon provides high porosity and increased specific surface area. Meanwhile, the HBP-s sample X-ray diffractogram also showed some sharp peaks indicating impurities. These are associated the presence of some high molecular weight volatiles, including magnesium (2θ = 36º; MgO; JCPDS card No.89-7746), potassium and calcium (2θ = 37º; CaO; JCPDSNo.82-1690). Specifically, calcium is commonly prone to $CaCO_3$ contamination, being one of the by-product in bamboo pyrolysis [18].

Table 3. XRD parameter of activated carbon monolith derived HBP-s

Samples	d_{002} (Å)	d_{100} (Å)	L_c(Å)	L_a (Å)	Lc/La
HBP-1	3.69	2.03	7.79	2.15	0.36
HBP-3	3.56	1.97	7.19	5.44	1.32

Table 3 showed the XRD parameters, including interlayer spacing (d_{002} and d_{100}) and micro crystallites dimension (L_c for average crystallite sizes and L_a for average graphene sheet) characterized by turbostratic crystallite structure. Furthermore, the interlayer spacing (d_{002}) was calculated using equation 1, where 3.56 Å and 3.69 Å were obtained for HBP-1 and HBP-2, respectively, indicating the high disorder of carbon atom with amorphous structure. For examples, activated carbon biomass derived from sago waste performed a d_{002} between 3.59 - 3.60 Å [39]. Also, the current investigation shows an inverse relationship between increased KOH concentration and average crystallites size, characterized by the decline from 7.79 to 7.19 Å. This phenomenon was due to the rearrangement of carbon atom during chemical activation at high temperatures of 700 ºC. In addition, the increase in the average graphene sheet from 2.15 to 5.44 Å, was attributed to the electronegative repulsion of carbon atom [40]. These data confirm the ability for lower crystallite size and higher graphene sheet to provide better specific surface area, corresponding to the Kumar empirical formula (S= 2 / (ρL_c)), where S denotes the predicted surface area, and ρ is the graphite density [41].

3.5 Energy Dispersive X-ray

The energy dispersive X-ray (EDX) was used to evaluate the chemical elements in HBP-s samples, as shown in Table 4. The process of carbonization and chemical activation with KOH have successfully converted biomass derived bamboo

into monolithic activated carbon with high carbon content, precisely ~84% and ~78% atomic weight for HBP-1 and HBP-2, respectively. Also, the samples showed high oxygen composition of over 10%. In addition, bamboo biomass is known to contain functional groups with a combination of carbon and oxygen, including phenol (C-OH), quinone (C=O) or ether (C-O-C), and carboxylic groups (COOH) [2]. However, the oxygen released during the carbonization process was due to low molecular weight and bad thermal stability [15], while carbon percentage decreased alongside the rise in KOH concentration. These results are associated with the attribution of alkali to the C and O bond. In addition, the higher oxygen content in HBP-3 possibly increases wettability and consequently ion diffusion into the electrode deep pores, due to higher amounts of oxygen functional groups [42].

The carbonization and chemical activation process reserve smaller amounts of volatiles, including magnesium, potassium and calcium [14]. Furthermore, the magnesium and calcium components were reduced, while potassium increased at higher KOH concentrations. These results are attributed to the chemical activation of KOH, which etched the bond of carbon-volatiles and increase K_2CO_3-occupied and K-bound [2], due to imperfect removal in the carbon samples [43].

Table 4. Chemical composition analysis from EDX.

Elements	HBP-1		HBP-3	
	Mass (%)	Atomic weight (%)	Mass (%)	Atomic weight (%)
Carbon	76.66	84.27	68.61	78.52
Oxygen	15.54	12.83	20.34	17.48
Magnesium	1.35	0.73	0.56	0.31
Potassium	5.05	1.70	10.50	3.69
Calcium	1.41	0.46	-	-
Total	100%			

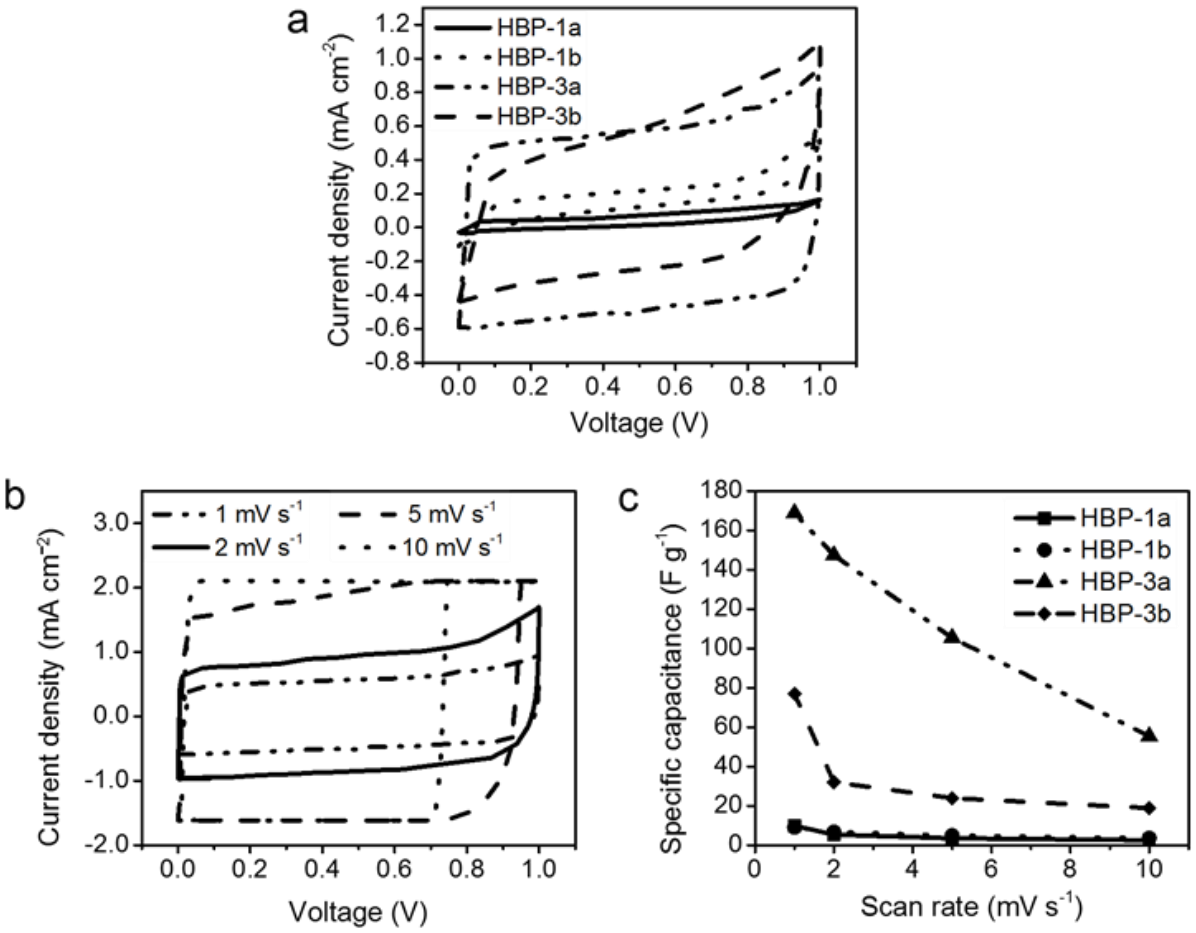

Fig. 5. Electrochemical measurements in a two-electrode system: (a) CV curves from HBP-s samples at a scan rate of 1 mV s^{-1}; (b) CV curve from HBP-3a at different scan rates; (c) the specific capacitance from HBP-s samples at different scan rate.

3.6 Electrochemical Performance

The electrochemical performance of HBP-s was evaluated using the cyclic voltammetry (CV) method, where the samples were prepared with two different thickness levels, including 0.2 mm (a) and 0.3 mm (b). Figure 5 (a) shows the evaluation process, where two-electrode configurations were used in 1 M H_2SO_4 electrolyte, at a scan rate of 1 mV s^{-1}. The results clearly shows the rectangular-like shape structure of the CV curves, typical for EDLC mechanism [29,44]. Furthermore, the specific capacitance (C_{sp}) was derived following equation 4, characterized by significant improvement from 9.87 to 168.80 F g^{-1} for HBP-1a and HBP-3a, respectively, with thickness of 0.2 mm. Therefore, an

increase in thickness to 3 mm also elevated the C_{sp} with varied KOH concentration at 9.13 and 77.03 F g^{-1} respectively for HBP-1b and HBP-3b. Based on these results, the specific capacitances reported are attributed to morphology structure and the presence of properly developed pores at higher alkali activation [26,32]. Hence, a change in electrode thickness is concluded to not significantly affect the capacitive behavior of 1 M KOH activation, while the specific capacitance dropped in treatments using the 3 M KOH. In summary, the thinner samples are estimated to provide much better electrochemical performance. This phenomenon is attributed to the lower internal resistance, resulting from the reduced electrode mass, and also the improved specific surface area accessibility, due to the decline in pore block quantity after polishing.

As shown in Fig. 5(b), the CV curves from HBP-3a were steady and rectangular-like at different scan rates, ranging from 1 to 5 mV s^{-1}. This was due to the presence of properly developed pore structure distribution. In addition, three-dimensional configurations with large macropores formations also tend to function as ion transport channels, needed for the ion diffusion maintenance at high charge/discharge rates [32]. Also, the flake structure with highly accessible surface enhances electrical conductivity, and consequently increase the number of ion pairs on the surface carbon [33,34].

Table 5. Electrochemical performance from variousactivated carbon-basedbiomassin two-electrode system.

Precursor	Activator	S_{BET} (m^2 g^{-1})	C_{sp} (F g^{-1})	Electrolyte	3D structure	Ref
Areca catechu husk	KOH	757	165	1 M H_2SO_4	No	[29]
Bamboo pieces	KOH	2221	79	3 M KOH	Yes	[18]
Bamboo fiber	KOH	2561	47	1 M Na_2SO_4	No	[25]
Banana stem	KOH	836	170	1 M H_2SO_4	No	[43]
Willow	-	739	93	6 M KOH	Yes	[16]
Poplar wood	KOH	1612	263	6 M KOH	Yes	[31]
Ceder sawdust	KOH	1185	244	1 M Na_2SO_4	Yes	[30]
Wild rice stem	KOH	1228	81	6 M KOH	No	[45]
Mangosteen peel	KOH	1270	83	6 M KOH	Yes	[46]
Bamboo shoot	KOH	3250	209	6 M KOH	No	[38]
Bamboo leaves	-	325	162	3 M KOH	No	[47]
Hierarchically Bamboo	KOH	155	169	Electrolyte	Yes	Current study

Fig. 5(c) shows the specific capacitance for HBP-s samples at different scan rate, and the optimized output was observed with HBP-3a at 147.38 F g^{-1} (87.31%) and 105.43 F g^{-1} (62.46%) for scan rate of 2 and 5 mV s^{-1}, respectively. These results confirms the ability for three-dimensional structures with macropores to provide high amount of accessibility for a specific surface area [16]. However, the values respectively remained at 2.56, 3.64, 55.36, and 18.92 F g^{-1} for HBP-1a, HBP-1b, HBP-3a and HBP-3b, at the highest rate of 10 mV s^{-1}. These capacitances are associated with the diffusion rate of ions into the deeper pore, as an increase in KOH concentration facilitates to maintain their values, resulting from the high amount of pores developed. Also, the drop is somewhat affiliated with the increase in electrode thickness, due to the ability for pore blocking phenomenon to reduce accessibility to a specific surface area. Furthermore, samples HBP-1a, HBP-1b, HBP-3a and HBP-3b, respectively demonstrated the energy density of 1.37, 1.27, 23.44, 10.69 Wh kg^{-1} for power density of 4.95, 4.57, 84.46, and 38.55 W kg^{-1}. These results are typical for activated carbon biomass electrodes, as bamboo based industrial by-products exhibits values in the term of energy density and power density of 9.5 Wh kg^{-1} and 25 W kg^{-1}, respectively [17]. Table 5 shows the electrochemical performance from some activated carbon-based biomass reported lasted, where HBP-s displays a high specific capacitance of 168.80 F. g^{-1} with energy density of 23.44 Wh kg^{-1} for power density of 84.46 W kg^{-1}.

4. Conclusion

Based on the results and discussion, activated carbon in the monolithic form was prepared from hierarchically bamboo stem to improve applicability as a supercapacitor electrode. This was achieved using the stem pellet, through two step carbonizations, assisted with chemical activation. Furthermore, samples activated with 3 M KOH showed better electrochemical performance than those produced with 1 M KOH activation in 1 M H_2SO_4 electrolyte, characterized by the highest specific capacitance of 168.8 F g^{-1}, energy and power density of 23.44 Wh kg^{-1} and 84.46 W kg^{-1}, respectively, despite the low specific surface area of 154.6 m^2 g^{-1}. The activated carbon monolithic obtained a three-dimensional pore structure with a flake, resulting in better electrical conductivity, while the high oxygen content causes an increase in wettability, needed for better ion adsorption in the aqueous electrolyte. In addition to specific surface area, electrode architecture plays a more significant role in electrochemical performance, which was better at a thickness of 0.2 mm than 0.3 mm. Therefore, thinner materials result in lower internal resistance, excellent ion adsorption, and also a promising electrochemical performance.

Acknowledgements

The authors are grateful to the DRPM Kemenristek-Dikti for funding in this second year Project of PD with contract number 396/UN.19.5.1.3/PT.01.03/2020 with the title “High-density micro-and nano carbon fiber made from biomass based materials for supercapacitor electrodes”.

References

1. S. Koohi-Fayegh, M.A. Rosen, *A review of energy storage types , applications and recent developments*, J. Energy Storage. 27 (2020) 101047.
2. Y. Wang, Q. Qu, S. Gao, G. Tang, K. Liu, S. He, C. Huang, *Biomass derived carbon as binder-free electrode materials for supercapacitors*, Carbon 155 (2019) 706–726.
3. K. Fic, A. Platek, J. Piwek, E. Frackowiak, *Sustainable materials for electrochemical capacitors*, Mater. Today. 21 (2018) 437–454.
4. P. Ratajczak, M.E. Suss, F. Kaasik, F. Béguin, *Carbon electrodes for capacitive technologies*, Energy Storage Mater. 166 (2018) 126–145.
5. X. Yang, B. Fei, J. Ma, X. Liu, S. Yang, G. Tian, Z. Jiang, *Porous nanoplatelets wrapped carbon aerogel by pyrolysis of regenerated bamboo cellulose aerogels as supercapacitor electrodes*, Carbohydr. Polym. 180 (2017) 385–392.
6. Z. Xin, W. Fang, L. Zhao, H. Chen, X. He, W. Zhang, *N-doped carbon foam constructed by liquid foam with hierarchical porous structure for supercapacitor*, J. Porous Mater. 25 (2018) 1521–1529.
7. X. Ma, C. Ding, D. Li, M. Wu, Y. Yu, *A facile approach to prepare biomass-derived activated carbon hollow fibers from wood waste as high-performance supercapacitor electrodes*, Cellulose. 25 (2018) 4743–4755.
8. J.P. Jyothibasu, D.W. Kuo, R.H. Lee, *Flexible and freestanding electrodes based on polypyrrole/carbon nanotube/cellulose composites for supercapacitor application*, Cellulose. 26 (2019) 4495–4513.
9. Y. Wu, J. Zhu, L. Huang, *A review of three-dimensional graphene-based materials: Synthesis and applications to energy conversion/storage and environment*, Carbon 143 (2019) 610–640.
10. E.E. Miller, Y. Hua, F.H. Tezel, *Materials for energy storage : Review of electrode materials and methods of increasing capacitance for supercapacitors*, J. Energy Storage. 20 (2018) 30–40.
11. M.A. Yahya, Z. Al-qodah, C.W.Z. Ngah, *Agricultural bio-waste materials as potential sustainable precursors used for activated carbon production : A review*, Renew. Sustain. Energy Rev. 46 (2015) 218–235.
12. M. Inagaki, H. Konno, O. Tanaike, *Carbon materials for electrochemical capacitors*, J. Power Sources. 195 (2010) 7880–7903.
13. P. Thomas, C.W. Lai, M. Rafie, B. Johan, *Recent developments in biomass-derived carbon as a potential sustainable material for super-capacitor-based energy storage and environmental applications*, J. Anal. Appl. Pyrolysis. 140 (2019) 54–85.
14. E. Azwar, W. Adibah, W. Mahari, J. Huang, *Transformation of biomass into carbon nanofiber for supercapacitor application : A review*, Int. J. Hydrogen Energy. 43 (2018) 20811–20821.
15. M. Danish, T. Ahmad, *A review on utilization of wood biomass as a sustainable precursor for activated carbon production and application*, Renew. Sustain. Energy Rev. 87 (2018) 1–21.
16. C. Jiang, G.A. Yakaboylu, T. Yumak, J.W. Zondlo, M. Edward, J. Wang, *Activated carbons prepared by indirect and direct CO2 activation of lignocellulosic biomass for supercapacitor electrodes*, Renew. Energy. 155 (2020) 38–52.
17. W. Tian, Q. Gao, Y. Tan, K. Yang, L. Zhu, C. Yang, H. Zhang, *Bio-inspired Beehive-like Hierarchical Nanoporous Carbon Derived from Bamboo-based Industrial Byproduct as High Performance Supercapacitor Electrode Material*, J. Mater. Chem. A. 3 (2015) 5656–5664.
18. G. Zhang, Y. Chen, Y. Chen, H. Guo, *Activated biomass carbon made from bamboo as electrode material for supercapacitors*, Mater. Res. Bull. 102 (2018) 391–398.
19. M. Fujishige, I. Yoshida, Y. Toya, Y. Banba, K. Oshida, Y. Tanaka, P. Dulyaseree, W. Wongwiriyapan, K. Takeuchi, *Preparation of activated carbon from Bamboo-cellulose fiber and its use for EDLC electrode material*, Biochem. Pharmacol. 5 (2017) 1801–1808.
20. C. Kim, J. Lee, J. Kim, K. Yang, *Feasibility of bamboo-based activated carbons for an electrochemical supercapacitor electrode*, 23 (2006) 592–594.
21. C. Yang, Y.S. Jang, H.K. Jeong, *Bamboo-based activated carbon for supercapacitor applications*, Curr. Appl. Phys. 14 (2014) 1616–1620.
22. H. Chen, D. Liu, Z. Shen, B. Bao, S. Zhao, L. Wu, *Functional biomass carbons with hierarchical porous structure for supercapacitor electrode materials*, Electrochim. Acta. 180 (2015) 241–251.
23. B. Lu, L. Hu, H. Yin, X. Mao, W. Xiao, D. Wang, *Preparation and application of capacitive carbon from bamboo shells by one step molten carbonates carbonization*, Int. J. Hydrogen Energy. 41 (2016) 18713–18720.
24. K. Li, W. Chen, H. Yang, Y. Chen, S. Xia, M. Xia, X. Tu, H. Chen, *Mechanism of biomass activation and ammonia modification for nitrogen-doped porous carbon materials*, Bioresour. Technol. 280 (2019) 260–268.
25. L. Ji, B. Wang, Y. Yu, N. Wang, J. Zhao, *N, S co-doped biomass derived carbon with sheet-like microstructures for supercapacitors*, Electrochim. Acta. 331 (2019) 135348.
26. G. Huang, Y. Liu, X. Wu, J. Cai, *Activated carbons prepared by the KOH activation of a hydrochar from garlic peel and their CO2 adsorption performance*, New Carbon Mater. 34 (2019) 247–257.
27. Y. Wen, T. Qin, Z. Wang, X. Jiang, S. Peng, J. Zhang, J. Hou, F. Huang, D. He, G. Cao, *Self-supported binder-free carbon fi bers / MnO2 electrodes derived from disposable bamboo chopsticks for high-performance supercapacitors*, J. Alloys Compd. 699 (2017) 126–135.
28. E. Taer, Sugianto, M.A. Sumantre, R. Taslim, Iwantono, D. Dahlan, M. Deraman, *Eggs Shell Membrane as Natural Separator for Supercapacitor Applications*, Adv. Mater. Res. 896 (2014) 66–69.
29. E. Taer, Apriwandi, R. Handayani, R. Taslim, Awitdrus, A. Amri, Agustino, I. Iwantono, *The Synthesis of Bridging Carbon Particles with Carbon Nanotubes from Areca catechu Husk Waste as Supercapacitor Electrodes*, Int. J. Electrochem. Sci. 14 (2019) 9436–9448.
30. L. Yang, Y. Feng, M. Cao, J. Yao, *Two-step preparation of hierarchical porous carbon from KOH-activated wood sawdust for supercapacitor*, Mater. Chem. Phys. 238 (2019) 121956.
31. M. Liu, K. Zhang, M. Si, H. Wang, L. Chai, *Three-dimensional carbon nanosheets derived from micro- morphologically regulated biomass for ultrahigh-performance supercapacitors*, Carbon 153 (2019) 707–716.
32. X. Wei, J. Wei, Y. Li, H. Zou, *Robust hierarchically interconnected porous carbons derived from discarded Rhus typhina fruits for ultrahigh capacitive performance supercapacitors*, J. Power Sources. 414 (2019) 13–23.
33. S. Sankar, A. Talha, A. Ahmed, A.I. Inamdar, H. Im, Y. Bin, Y. Lee, D. Young, S. Lee, *Biomass-derived ultrathin mesoporous graphitic carbon nano fl akes as stable electrode material for high-performance supercapacitors*, Mater. Des. 169 (2019) 107688.
34. G. Zhang, H. Chen, W. Liu, D. Wang, Y. Wang, *Bamboo chopsticks-*

derived porous carbon microtubes/flakes composites for supercapacitor electrodes, Mater. Lett. 185 (2020) 359–362.

35. R.T. Ayinla, J.O. Dennis, H.M. Zaid, Y.K. Sanusi, F. Usman, L.L. Adebayo, *A review of technical advances of recent palm bio-waste conversion to activated carbon for energy storage*, J. Clean. Prod. 229 (2019) 1427–1442.
36. T. Yumak, G.A. Yakaboylu, O. Oginni, K. Singh, E. Ciftyurek, E.M. Sabolsky, *Comparison of the electrochemical properties of engineered switchgrass biomass-derived activated carbon-based EDLCs*, Colloids Surfaces A. 568 (2020) 124150.
37. D. Wang, L. Xu, J. Nai, X. Bai, T. Sun, *Morphology-controllable synthesis of nanocarbons and their application in advanced symmetric supercapacitor in ionic liquid electrolyte*, Appl. Surf. Sci. 473 (2019) 1014–1023.
38. G. Huang, Y. Wang, T. Zhang, X. Wu, J. Cai, *High-performance hierarchical N-doped porous carbons from hydrothermally carbonized bamboo shoot shells for symmetric supercapacitors*, J. Taiwan Inst. Chem. Eng. 96 (2019) 672–680.
39. E. Taer, A. Afrianda, R. Taslim, A. Agustino, R. Farma, *Production of Activated Carbon Electrodes from Sago Waste and its application for an Electrochemical Double-Layer Capacitor*, 13 (2018) 10688–10699.
40. J. Serafin, M. Baca, M. Biegun, E. Mijowska, R.J. Kale, *Direct conversion of biomass to nanoporous activated biocarbons for high CO2 adsorption and supercapacitor applications*, Appl. Surf. Sci. 497 (2019) 143722.
41. K. Kumar, R. Saxena, R. Kothari, D. Suri, K. Kaushik, J. Bohra, *Correlation between adsorption and x-ray diffraction studies on viscose rayon based activated carbon cloth*, Carbon 35 (1997) 1842–1844.
42. X. Song, X. Ma, Y. Li, L. Ding, R. Jiang, *Tea waste derived microporous active carbon with enhanced double-layer supercapacitor behaviors*, Appl. Surf. Sci. 487 (2019) 189–197.
43. E. Taer, R. Taslim, W.S. Mustika, B. Kurniasih, Agustino, A. Afrianda, Apriwandi, *Production of an activated carbon from a banana stem and its application as electrode materials for supercapacitors*, Int. J. Electrochem. Sci. 13 (2018) 8428–8439.
44. S. Ahmed, M. Rafat, A. Ahmed, *Nitrogen doped activated carbon derived from orange peel for supercapacitor application*, Adv. Nat. Sci. 9 (2018) 035008.
45. Q. Tian, X. Wang, X. Xu, M. Zhang, L. Wang, X. Zhao, Z. An, H. Yao, J. Gao, *A novel porous carbon material made from wild rice stem and its application in supercapacitors*, Mater. Chem. Phys. 213 (2018) 267-276.
46. Y. Li, X. Wang, M. Cao, *Three-dimensional porous carbon frameworks derived from mangosteen peel waste as promising materials for CO_2 capture and supercapacitors*, J. CO2 Util. 27 (2018) 204–16.
47. Q. Wang, Y. Zhang, H. Jiang, C. Meng, *In-situ grown manganese silicate from biomass-derived heteroatom-doped porous carbon for supercapacitors with high performance*, J. Colloid Interface Sci. 534 (2018) 142-155.